# A single-atom library for guided monometallic and concentrationcomplex multimetallic designs

Lili Han<sup>1†</sup>, Hao Cheng<sup>1†</sup>, Wei Liu<sup>2†</sup>, Haoqiang Li<sup>2</sup>, Pengfei Ou<sup>3</sup>, Ruoqian Lin<sup>4</sup>, Hsiao-Tsu Wang<sup>5</sup>, Chih-Wen Pao<sup>6</sup>, Ashley R. Head<sup>7</sup>, Chia-Hsin Wang<sup>6</sup>, Xiao Tong<sup>7</sup>, Cheng-Jun Sun<sup>8</sup>, Way-Faung Pong<sup>5</sup>, Jun Luo<sup>2,9</sup>\*, Jin-Cheng Zheng<sup>10,11</sup>\*, Huolin L. Xin<sup>1</sup>\*

- 1. Department of Physics and Astronomy, University of California, Irvine, CA 92697, USA.
- 2. School of Materials Science and Engineering, Tianjin Key Lab of Photoelectric Materials & Devices, Tianjin University of Technology, Tianjin 300384, China.
- 3. Department of Mining and Materials Engineering, McGill University, Montreal H3A 0C5, Canada.
- 4. Center for Functional Nanomaterials, Brookhaven National Laboratory, Upton NY 11973, USA.
- 5. Department of Physics, Tamkang University, New Taipei City 251301, Taiwan.
- 6. National Synchrotron Radiation Research Center, Hsinchu 30076, Taiwan.
- 7. Center for Functional Nanomaterials, Brookhaven National Laboratory, Upton NY 11973, USA.
- 8. X-ray Science Division, Argonne National Laboratory, Lemont, IL 60439, USA.
- 9. Shenzhen Institute for Advanced Study, University of Electronic Science and Technology of China, Shenzhen 518110, China.
- 10. Department of Physics and Fujian Provincial Key Laboratory of Theoretical and Computational Chemistry, Xiamen University, Xiamen 361005, China.
- 11. Department of Physics and Department of New Energy Science and Engineering, Xiamen University Malaysia, 439000 Sepang, Selangor, Malaysia.

\*Corresponding author. Email: jluo@tjut.edu.cn (J.L.); jczheng@xmu.edu.cn (J.Z); huolin.xin@uci.edu (H.L.X.).

†These authors contributed equally to this work.

Abstract: Atomically dispersed single-atom catalysts (SACs) have the potential to bridge heterogeneous and homogeneous catalysis. Dozens of SACs have been developed and they exhibit notable catalytic activity and selectivity that are not achievable on metal surfaces. Although promising, there is limited knowledge about the boundaries for the monometallic single-atom phase space, not to mention multimetallic phase spaces. Herein, SACs based on 37 monometallic elements were synthesized using a dissolution-and-carbonization method, characterized, and analyzed to build the largest reported library of SACs. In conjunction with in-situ studies, we uncovered unified principles on the oxidation state, coordination number, bond length, coordination element, and metal loading of single atoms to guide the design of SACs with atomically dispersed atoms anchored on N-doped carbon. We utilized the library to open up complex multimetallic phase spaces for SACs and demonstrate there is no fundamental limit on using single atom anchor sites as structural units to assemble concentration-complex SAC materials with up to 12 different elements. Our work offers a single-atom library spanning from monometallic to concentration-complex multimetallic materials for the rational design of SACs.

#### **Main Text:**

Single-atom catalysts (SACs), with isolated metal atoms anchored on solid substrates, possess the combined merits of easy separation, excellent recyclability and easy immobilization of heterogeneous catalysts, as well as highly uniform active centers, tunable coordination environment and high atom utilization efficiency of homogeneous catalysts<sup>1–3</sup>. Thus, SACs hold great promise for bridging the gap between heterogeneous catalysis and homogeneous one. Moreover, SACs offer a fundamental platform to probe the catalytic structure–performance relationships as well as to investigate the catalytic mechanisms at the atomic scale<sup>4</sup>. In the past few

years, dozens of SACs have been developed for electrocatalysis, thermocatalysis, photocatalysis, and energy storage as well as organic electrosynthesis, and they exhibit notable catalytic activity and selectivity that are not achievable on metal surfaces<sup>1–21</sup>.

Despite the recent surge in SAC research, several grand challenges remain. First, a set of unified guiding principles that govern the formation of SACs is lacking. In particular, because different metallic centers have different chemical and electronic properties, a guiding principle for the synthesis of one SAC cannot be simply extrapolated to another. Second, it remains difficult to regulate local structures of SACs, including bond length, oxidation state, coordination number (*CN*), and coordination anions. This is mainly due to the lack of a comprehensive understanding of SAC formation mechanisms. Third, it is difficult to control the loading of metal single atoms (SAs) since SAs tend to aggregate into nanoclusters/particles due to the Gibbs-Thomson effect<sup>18,19</sup>. It is believed that nitrogen plays an important role in anchoring SAs<sup>20</sup>; however, simply increasing nitrogen content does not always lead to higher SA loading<sup>11</sup>. Fourth, to date, a knowledge gap exists in how to marry different elemental metal sites into one SAC system and open up concentration-complex multimetallic phase spaces for SACs that are exponentially more complex than conventional SACs containing only one or two metallic elements (termed mono- or dimetallic SACs).

### Synthesis and characterization of SACs

Here, to meet these challenges, we synthesized a large library of monometallic SACs—37 different metallic elements supported on carbon—using the same dissolution-and-carbonization method (Fig. 1a, b, Supplementary Figs. 1, 2 and Supplementary Table 1). Most of these SACs are of value to electrochemical applications, as supported by their catalytic performances reported in our

previous studies<sup>8–10</sup>. We have also realized the formation of multimetallic SACs, such as 2-, 8-, and 12-metallic SACs, by the same synthetic method (Supplementary Table 2).

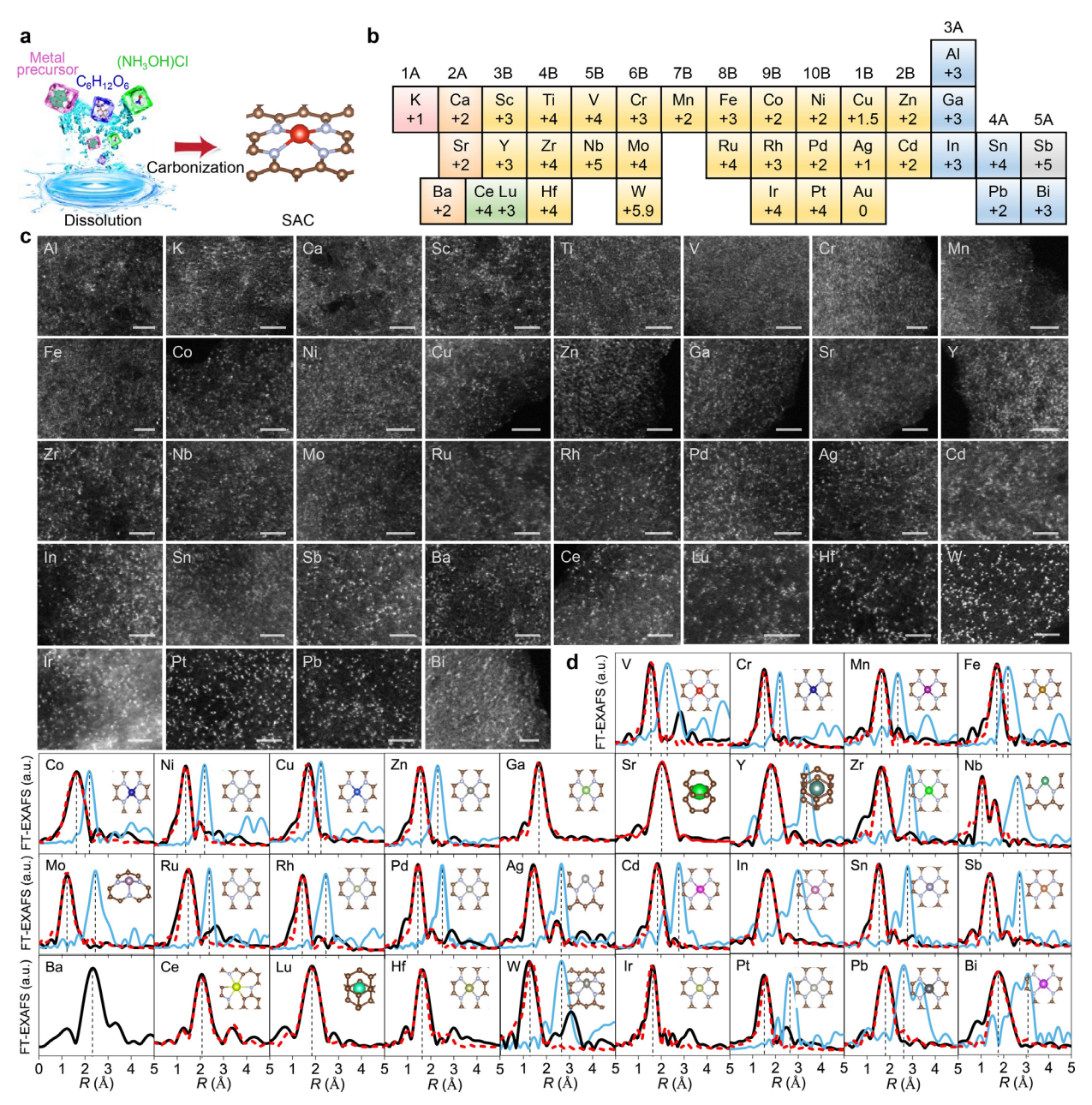


Fig. 1 | Synthesis and characterization of monometallic SACs. a, Schematic of SAC synthesis. b, 37 metallic elements and their average valences for the SACs. c, Aberration-corrected HAADF-STEM images (see Supplementary Fig. 38 for Au SAC). The scale bar is 2 nm. d, FT-EXAFS spectra for SACs (black), fittings (red) and reference foils (dodger blue). The Y-axis values were normalized by the intensity of main peaks for comparison. The insets in (d) show the corresponding atomic structures of SACs for the EXAFS fittings.

Our monometallic SACs were characterized by X-ray diffraction (XRD), scanning electron microscopy (SEM), transmission electron microscopy (TEM), aberration-corrected high-angle annular dark-field scanning transmission electron microscopy (HAADF-STEM), energy-dispersive spectroscopy (EDS), X-ray photoelectron spectroscopy (XPS), synchrotron radiation-based soft X-ray absorption spectroscopy (XAS), and X-ray absorption fine structure (XAFS) spectroscopy (Fig. 1c, d and Supplementary Figs. 3–40). Each SAC in Fig. 1 was strictly screened out by, first, synthesizing samples with various metal precursor ratios as listed in Supplementary Table 1, second, selecting samples that do not show XRD peaks for metal-related crystals, third, selecting atomically dispersed SA samples using aberration-corrected HAADF-STEM, and, fourth, confirming the atomic dispersion by XAFS until the SAC sample with the largest metal precursor ratio is found.

The SAs in each SAC are uniformly distributed both on the surface and in the bulk of the SAC with a similar bonding environment, as evidenced by the soft XAS spectra for SAs in the surface-sensitive total electron yield (TEY) and the bulk-sensitive partial fluorescence yield (PFY) modes<sup>22</sup> in Supplementary Figs. 4, 6–8 and 10–16. The oxidation states of the SAs were determined by XPS, and the average values are shown in Fig. 1b and Supplementary Table 3. Further, the oxidation states of 3d transition metal centers were cross-validated by soft XAS (Supplementary Figs. 4–8). The fittings of Fourier-transformed (FT) extended X-ray absorption fine structure (EXAFS) spectra for the SACs were performed with the models in the insets of Fig. 1d (note that it is difficult to discern C, N and O coordinates by EXAFS fitting due to their similar atomic numbers). The final fitting results are shown in Fig. 1d and Supplementary Table 4.

## Correlation for monometallic SAC properties

The local environment of each SA element is key because it determines the catalytic performance of the SAC. It includes the bond length of the SA to its first-shell neighbors, the *CN* and the coordination elements. The bond lengths and the *CNs* extracted from the EXAFS fitting parameters in Supplementary Table 4 are plotted in Fig. 2a, b, showing that the bond length initially decreases, then increases, and subsequently oscillates from left to right across each row in Fig. 1b. Based on the correlation analyses for the SAC properties in Fig. 2c, d, it is found that the bond length has a negative correlation with the oxidation state (Supplementary Fig. 41) and a positive correlation with the *CN*. This finding shows a general principle that a larger oxidation state and a smaller *CN* lead to a smaller bond length and vice versa<sup>23,24</sup>. For example, the SA elements in the 5B, 6B and 10B groups lose more outer electrons or have smaller *CNs*, leading to shorter bond lengths (shaded areas in Fig. 2a, b and Supplementary Fig. 41).

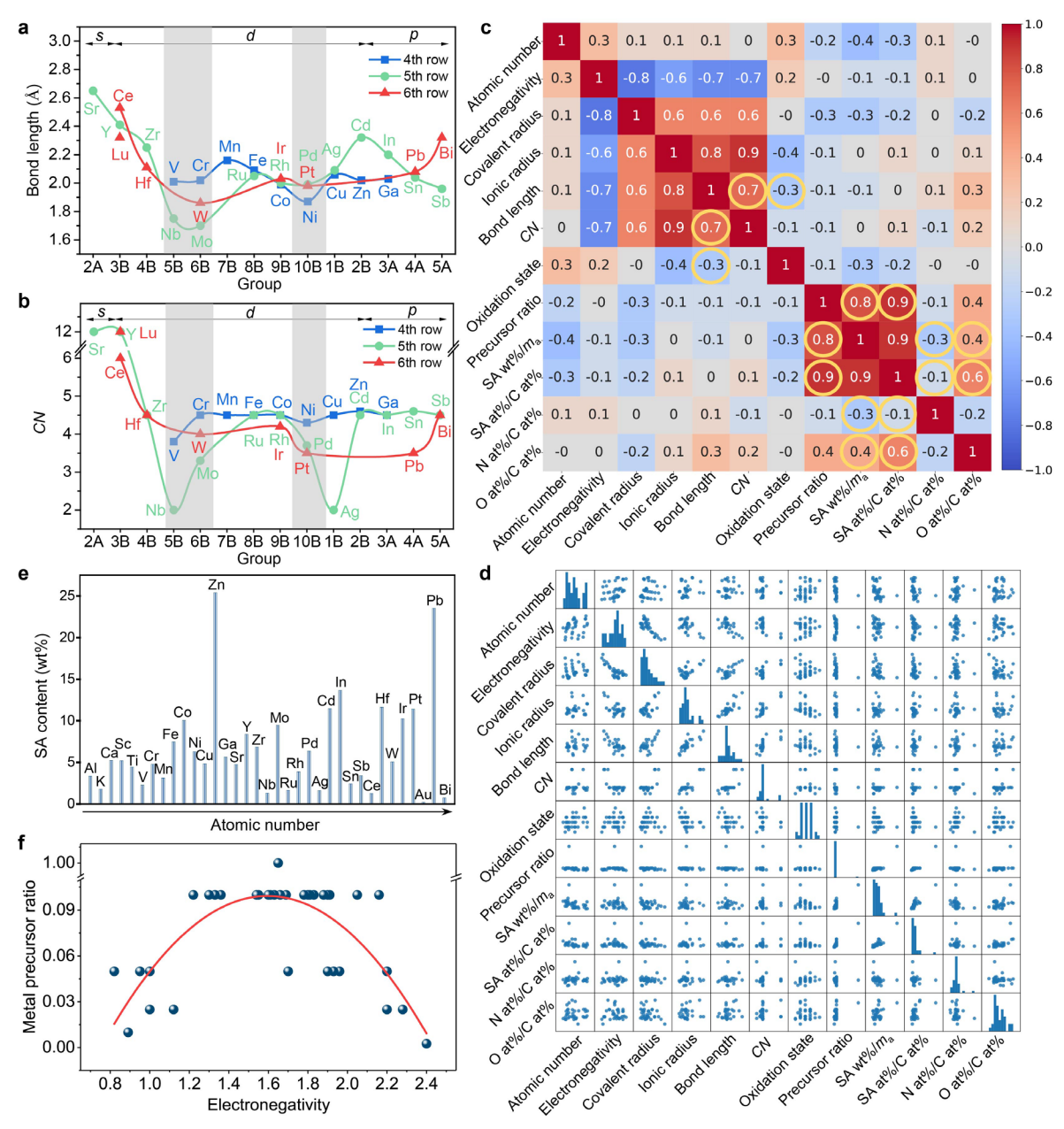


Fig. 2 | Correlation analyses for the monometallic SAC properties. a, Bond lengths of SAs to their first-shell elements. b, CN values for SAs. c, Correlation of SAC properties, where a more positive value represents a more positive correlation and vice versa. SA wt%/ $m_a$ , SA at%/C at%, N at%/C at% and O at%/C at% denote SA weight percent determined by ICP-MS over relative atomic mass, SA atomic percent over C atomic percent determined by XPS, N atomic percent over C atomic percent determined by XPS, respectively. d, Scattering matrix of correlation for SAC properties. The scatter diagram at the matrix unit shows the correlation of two SAC properties, while the histogram at the diagonal represents the frequency distribution of each SAC property. e, SA loadings in SACs, determined by ICP-MS. f, Dependence of the largest SAC metal precursor ratios on electronegativity.

Furthermore, we synthesized and characterized various SACs (including Cr, Fe, Co, Ni, Cu, Zn, Ga, Y, Ru, Pd, Cd, Sb, Ir, Pt and Bi) with lower loading of SAs to validate the trends (Supplementary Figs. 10, 12–17, 19, 23, 25, 27, 30, 36, 37 and 40, as well as Supplementary Table 5). The results show that the bond length, coordination number, and oxidation state of the SAs with lower loading have trends similar to those with the original ones (Supplementary Fig. 42). This suggests that the general trends can be referred to by the set of samples with lower loading.

To validate whether the trends still hold with a different synthetic method, we prepared numerous SACs, including Co, Cu, Ga, Y, Rh, Lu, Ir and Bi supported on metal-organic framework (MOF) substrates, by another synthetic method (abbreviated as the MOF method) that has been widely used in SAC research<sup>25,26</sup>, and we also carefully characterized them (Supplementary Figs. 43–50 and Supplementary Table 6). Comparison of bond lengths, CN values, and oxidation states of SAs synthesized by the dissolution-and-carbonization and the MOF methods in Supplementary Fig. 51 shows that the bond length, coordination number, and valence state of the SACs obtained by the MOF method have trends similar to those by the dissolutionand-carbonization method, and a few features such as the bond length of Y, the coordination numbers of Co and Cu, as well as the oxidation state of Cu, deviate a little from the trends. Even though the principles we extracted can be referred to by those of another method for the SAC systems with N-doped carbon to some extent, they are not in full accord due to the complexity of the synthetic environment. For example, the various synthetic factors such as types of carbon/nitrogen/metal precursor, heat-treatment conditions, temperature, etc. could affect the properties of the mononuclear sites in SACs<sup>27</sup>.

Moreover, to further explore the local environment of SAs, we carried out X-ray absorption near edge structure (XANES) fittings for 21 four-coordinated SAs with MN<sub>4</sub> and MO<sub>4</sub> (M=metal) structures (Supplementary Figs. 52–54). The fitting analyses in Supplementary Fig. 55 show that V, Cr, Fe, Cu, Ga, Zr, Ru, In, Sn and Sb SAs have better MN<sub>4</sub> fitting than MO<sub>4</sub>, and Mn, Co, Ni, Zn, Rh, Pd, Cd, Ir, Pt, Pb and Bi SAs have better MO<sub>4</sub> fitting than MN<sub>4</sub>.

The SA loading is another key factor because it determines the density of active sites for catalytic applications. In this work, the SA loading in the bulk and on the surface of each SAC was measured by inductively coupled plasma mass spectrometry (ICP-MS) and XPS, respectively, and the results are shown in Fig. 2e, Supplementary Fig. 56a,b, and Supplementary Table 3. Based on the correlation analyses in Fig. 2c, d, it is found that the loadings are most positively correlated to the largest metal precursor ratios, indicating that the loading can be controlled by adjusting the ratio, which is also a general principle. To rationally analyze the ratios, we plotted the curve for the largest SAC metal precursor ratio vs electronegativity (Fig. 2f) and found that as the electronegativity increases, the ratio initially increases, then flattens and finally decreases, suggesting a parabolic relationship (red line in Fig. 2f). By contrast, the parabolic relationship between electronegativity and loading amount (SA wt%/m<sub>a</sub>) (Supplementary Fig. 57) is not so obvious as the one between electronegativity and metal precursor ratio (Fig. 2f). This is because the SA wt%/ma is not always proportional to the metal precursor ratio due to the different vaporizations of different metal precursors. These findings indicate that the upper threshold of metal precursor ratio for the synthesis of SACs can be quantitatively predicted by the corresponding metal electronegativity, which is an important general principle. Moreover, the loadings have a large positive correlation with the O content in SACs and a small but negative correlation with the N content in SACs, which is another general principle. This surprising finding

suggests that the oxygen content might play a more important role in controlling SA loading compared to nitrogen content. This might also explain why the strategy of increasing nitrogen content might fail to increase the SA loading. To understand the convoluted roles of oxygen and nitrogen in anchoring SAs, we investigated the local structure and bonding evolution during SAC synthesis by in-situ XAFS and in-situ XPS (Fig. 3) together with temperature-dependent thermogravimetric analysis (TGA), Raman spectroscopy, and XRD (Supplementary Fig. 58).

#### Formation mechanism for monometallic SACs

For the in-situ study, we chose the synthesis of Mo SAC as an example for metals with high electronegativity (Fig. 3a-i). As shown in Fig. 3e, with increasing temperature, the ammonium molybdate first transforms into a local structure based on one Mo atom coordinating with six O atoms, as evidenced by analyses for the XANES and EXAFS spectra at 200 °C in Fig. 3a-d and the Mo-O bonding found in Fig. 3g. Then, longer Mo-O bonds obtained from the XANES and EXAFS fittings in Fig. 3b, d, shown as on top and bottom bonds in Fig. 3e, are expected to break first. Subsequently, the O atoms on the other four Mo-O bonds are successively replaced by N or C to form Mo $X_2$ O (X=N or C), evidenced by analyses for the XANES and EXAFS spectra at 400 °C that are fitted with the MoC<sub>2</sub>O moiety found in Fig. 3a–d and the Mo-N and Mo-C bonds found in Fig. 3h, i. Finally, a MoC<sub>2</sub>X structure with a Mo valence state of +4 is formed, demonstrated by analyses for XANES and EXAFS spectra at 600 °C that are fitted with the MoC<sub>2</sub>N moiety found in Fig. 3a–d, the absence of the Mo-O bond in Fig. 3g, and the Mo oxidation state of +4 in Fig. 3f (see Supplementary Fig. 59 and Supplementary Table 7 for the XANES fitting details). The local structure evolution dynamics determined from XAFS and XPS were cross-validated by TGA, Raman and XRD analyses (Supplementary Fig. 58).

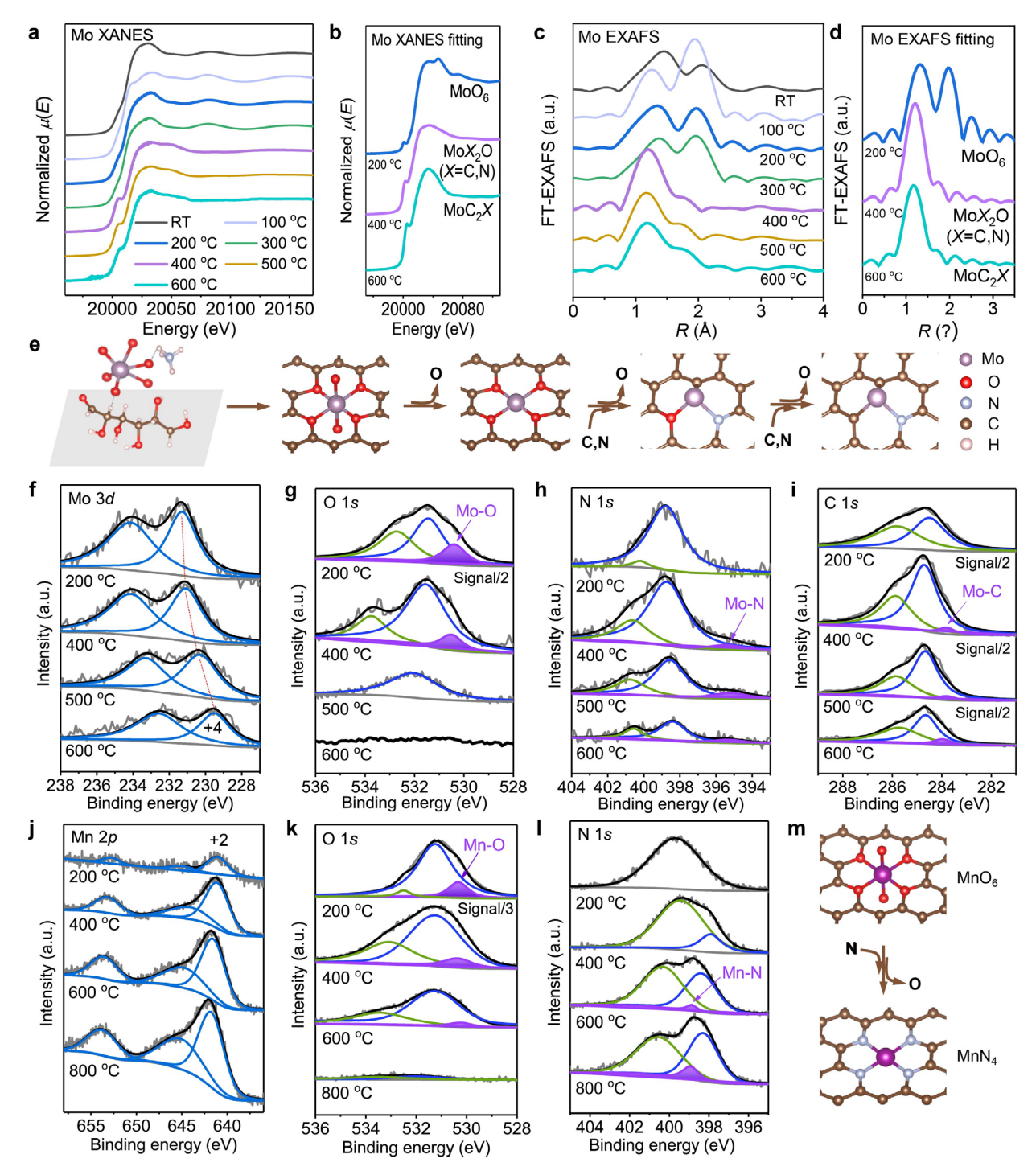


**Fig. 3** | **Temperature-induced evolution dynamics for SACs. a**, In-situ Mo *K*-edge XANES spectra for the Mo SAC synthesis. **b**, XANES fitting curves with MoO<sub>6</sub>, MoC<sub>2</sub>O and MoC<sub>2</sub>N moieties. **c**, In-situ Mo *K*-edge FT-EXAFS spectra. **d**, EXAFS fitting curves with MoO<sub>6</sub>, MoC<sub>2</sub>O and MoC<sub>2</sub>N moieties. **e**, Schematic of atomic structure evolution during Mo SAC formation. As the temperature increases, the two longer Mo-O bonds of the local structure with one Mo atom coordinating with six O atoms break first, forming a MoO<sub>4</sub> structure. Subsequently, the O atoms on the MoO<sub>4</sub> are successively replaced by N or C to form Mo*X*<sub>2</sub>O (*X*=N or C). **f**, In-

situ Mo 3*d*, **g**, O 1*s*, **h**, N 1*s* and **i**, C 1*s* XPS spectra for the Mo SAC synthesis. **j**, In-situ Mn 2*p*, **k**, O 1*s*, and **l**, N 1*s* XPS spectra for the Mn SAC synthesis. **m**, Schematic of the structural conversion of MnO<sub>6</sub> to MnN<sub>4</sub>. At 200 °C, one Mn atom coordinates with six O atoms. When the temperature is increased to 800 °C, the Mn-O bond is displaced by the Mn-N bond, forming an MnN<sub>4</sub> structure.

We take the synthesis of Mn SAC as an example for metals with medium electronegativity (Fig. 3j–m and Supplementary Fig. 60). The Mn atom first forms its coordination with six O atoms, as evidenced by the analyses for the XANES and EXAFS spectra at 200 °C (Supplementary Fig. 60a, b) and the Mn-O bonding (Fig. 3k). Unlike the Mo SAC synthesis, the Mn-O bond is still present in the sample at 600 °C (Fig. 3k). Furthermore, when the temperature is increased to 800 °C, the Mn-O bond disappears (Fig. 3k), and the Mn-N bond remains (Fig. 3l). The XANES and EXAFS spectra match well with those for the MnN<sub>4</sub> structure (Supplementary Fig. 60c,d). These findings are consistent with the analyses of the in-situ O and N *K*-edge soft XAS spectra in Supplementary Fig. 61.

The evolution dynamics for the synthesis of the Mo and Mn SACs illustrate that the center metal atoms coordinate with O at low temperatures, the coordinated O is successively replaced by N or C at high temperatures, and the final coordination environment of SACs depends on not only the SA species but also the terminal temperature. This finding explains why the SA affinities towards N and O based on the formation energies of MN<sub>4</sub> and MO<sub>4</sub> from density functional theory (DFT) thermodynamics calculations at 0 K (see Methods section and Supplementary Fig. 62 for details) deviate from those based on the XANES fitting with MN<sub>4</sub> and MO<sub>4</sub> from the more complicated temperature-dependent competence between thermodynamics and kinetics during the nonequilibrium synthesis process (Supplementary Fig. 63). It is worth noting that in most carbon-based SA systems, oxygen quickly evaporates at 800 °C or above<sup>28</sup>. If we had built the library at

high temperatures, we would be less likely to reveal the positive correlation between SA loading and oxygen. It is also important to note that correlation does not mean causality. Our in-situ investigation suggests indeed that oxygen plays an important role in anchoring SAs on carbon at low temperatures and nitrogen only replaces oxygen at higher temperatures as oxygen evaporates more easily than nitrogen<sup>28</sup>.

## Concentration-complex multimetallic SACs

Based on the synthesis of the 37 mono-element SACs, the library suggests that the dissolutionand-carbonization strategy enables the chelation of different metal centers on glucose and their separation by glucose backbones, and, thus, we infer that the strategy can facilitate the formation of concentration-complex multiple metallic-element SAs in one sample. Then, by controlling the species and concentrations of multiple metal precursors, multimetallic SAs are successfully achieved, such as 2-, 8-, and 12-metallic SACs, with their atomic dispersions verified by aberration-corrected STEM imaging and XAFS measurement (Fig. 4a–f and Supplementary Figs. 64–67). The 8- and 12-metallic SACs with high metal loading, are extremely difficult to synthesize because each metallic atom in the 8- and 12-metallic SACs must overcome the aggregations with not only themselves but also any one of the other metallic atoms. However, we synthesized an 8metallic SAC containing V, Cr, Mn, Fe, Co, Ni, Cu, and Zn (Supplementary Fig. 65) and a 12metallic SAC with Sc, Mn, Fe, Co, Ni, Cu, Zn, Y, Zr, Pd, Hf, and W (Fig. 4 and Supplementary Figs. 66–68). Atomic-resolution STEM images show that the SAs are all atomically and uniformly dispersed across the carbon support (Fig. 4a-d), which is further confirmed by the XAFS spectra in Fig. 4e and Supplementary Fig. 66, as well as the EXAFS fitting results in Supplementary Fig. 67 and Supplementary Table 8. The content and valence state of the SAs were determined by ICP-MS and XPS, respectively, as shown in Fig. 4f, Supplementary Fig. 68 and Supplementary Table 2. The total metal loading of the 12-metallic SAC reaches 7.53 wt%, which is considered a high value. These results demonstrate that there is no fundamental limit on using SA anchor sites as structural units to assemble concentration-complex multimetallic SAC materials.

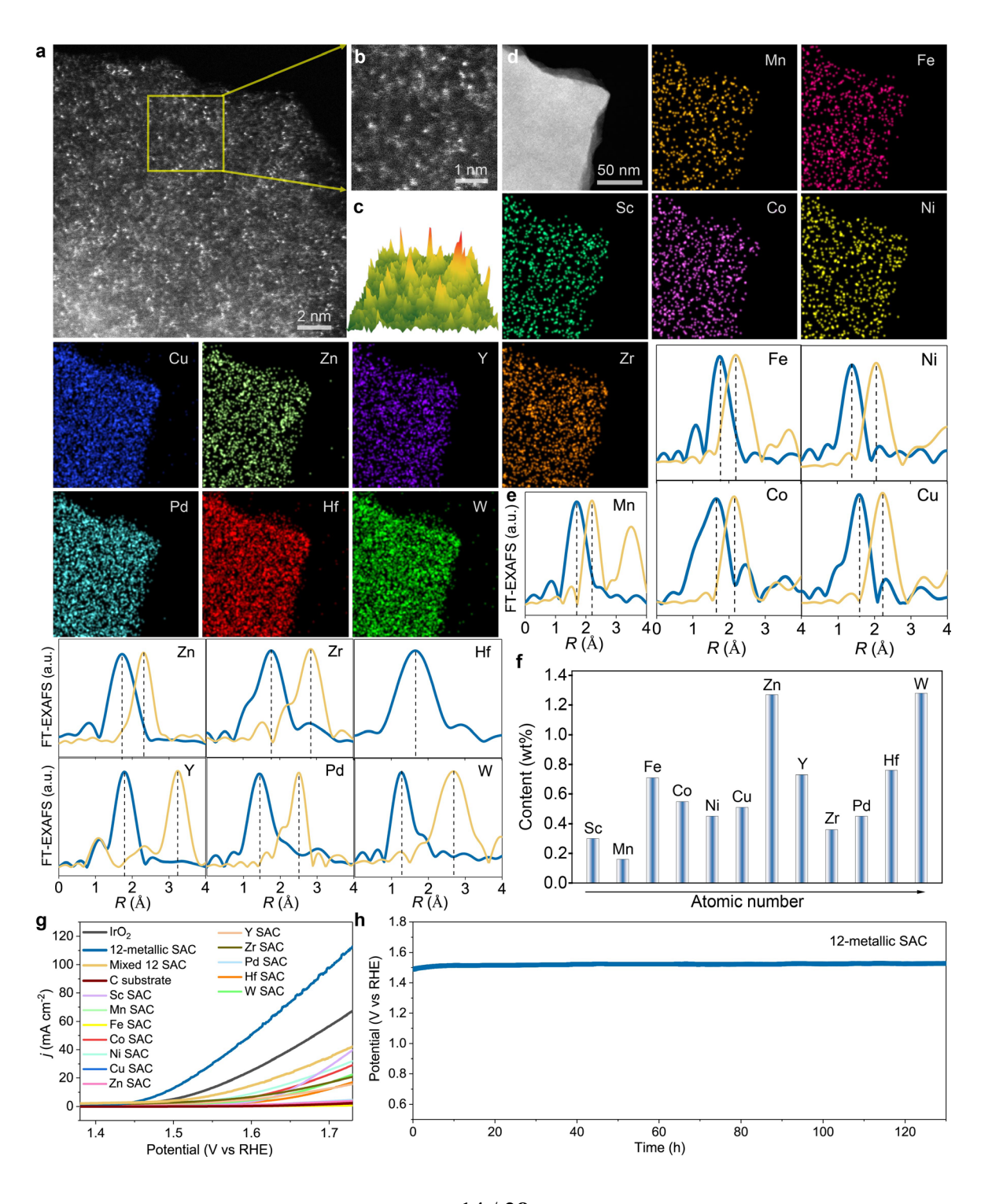


**Fig. 4** | Characterization and OER performance of concentration-complex SAC containing 12 different metallic elements. **a**, Atomic-resolution HAADF-STEM images. **b**, Close view of the boxed region in (**a**). **c**, Pseudocolor surface plot of a randomly selected area in (**a**), showing SAs with various contrasts in the matrix. **d**, HAADF-STEM image and EDS elemental maps. **e**, FT-EXAFS spectra for SAs (turquoise) and corresponding reference foils (orange). The Y-axis values were normalized by the intensity of main peaks for comparison. **f**, Content of each metallic element determined by ICP-MS. **g**, Linear sweep voltammetry (LSV) curves of the 12-metallic SAC, the mixed 12 monometallic SAC, the individual monometallic SACs, the C substrate, and commercial IrO<sub>2</sub>. **j** is current density. RHE denotes reversible hydrogen electrode. **h**, Chronopotentiometric curve obtained with the 12-metallic SAC.

Notably, the 12 different elements in the 12-metallic SAC, different from the mechanically mixed 12 monometallic SA material, are homogeneously affixed to the same matrix with atomiclevel distribution. To explore their electrocatalysis, we performed electrocatalytic oxygen evolution reaction (OER) experiments on the 12-metallic SAC, the corresponding mechanically mixed 12 monometallic SAC and the corresponding individual monometallic SACs. Representative OER currents of the samples were measured in 0.1 M KOH aqueous electrolyte at a scan rate of 10 mV s<sup>-1</sup>. The current density, mass activity and turnover frequency (TOF) of the 12-metallic SAC are higher than those of the mixed and individual monometallic SACs at the same potentials, meaning the higher activity of the 12-metallic SACs for OER (Fig. 4g and Supplementary Fig. 69). Also, the 8-metallic SAC has a higher OER activity than its corresponding mixed monometallic SAC (Supplementary Fig. 70). To explore the active species in the 12metallic SAC for OER, we tested OER activities based on Fe, Co, and Ni groups which have been reported to have promising performances for OER<sup>29-32</sup>, such as Fe-Ni SAC, Fe-Co SAC, Co-Ni SAC, Fe-Co-Ni SAC, Fe-Co-W SAC, Fe-Co-Ni-Cu SAC, Fe-Co-Ni-Mn SAC. The results of OER activity in Supplementary Fig. 71 demonstrate the OER activity order: Fe-Ni SAC < Fe-Co SAC < Co-Ni SAC; Fe-Co-W SAC < Fe-Co-Ni SAC; Fe-Co-Ni-Cu SAC < Fe-Co-Ni-Mn SAC; Co-Ni

SAC< Fe-Co-Ni SAC < Fe-Co-Ni-Mn SAC. From the order, the OER activity of the quadmetallic Fe-Co-Ni-Mn SAC is better than that of the trimetallic Fe-Co-Ni SAC and far better than that of the bimetallic Co-Ni SAC. The activity of 12-metallic SAC is better than that of the quadmetallic Fe-Co-Ni-Mn SAC. Therefore, we conclude that the multi-element synergistic interaction in the 12-metallic SAC can further enhance the OER activity. Moreover, we ran OER on the 12-metallic SAC at a constant current of 10 mA cm<sup>-2</sup> continuously for 130 hours. No appreciable increase in potential was observed in this time interval (Fig. 4h), which indicates the high stability of the 12-metallic SAC for OER. The stability of OER electrolysis can be assigned to the stable structure resulting from the strong bonding between the metals and the support<sup>33</sup>.

In summary, we have built a single-atom library ranging from monometallic to concentration-complex multimetallic materials. The big data analyses of the correlation of SAC properties in the library not only provide unified principles to understand the nature of active sites in different kinds of SACs, but also inspire a deeper insight into the SAC formation mechanism. This work may potentially open up exponentially more complex multimetallic phase spaces for SACs and inspire new research areas for SAC discovery and optimization, where the elemental composition of SACs can be leveraged in controlling SAC synthesis and activity.

## Acknowledgments

This work was supported by the National Science Foundation under award number CHE-1900401 and the start-up funding of H.L.X. This research used resources of the Center for Functional Nanomaterials as well as 7-BM and 23-ID-2 beamlines of the National Synchrotron Light Source II, which are two U.S. Department of Energy (DOE) Office of Science User Facilities operated for the DOE Office of Science by Brookhaven National Laboratory under Contract No. DE-

SC0012704. This research also used resources of the Advanced Photon Source, a U.S. DOE Office of Science User Facility operated for the DOE Office of Science by Argonne National Laboratory under Contract No. DE-AC02-06CH11357. The XAFS/EXAFS spectra obtained from beamline TPS 44A National Synchrotron Radiation Research Center (NSRRC) and the soft XAS data obtained from beamline TLS-BL24A at NSRRC is appreciated. This work made use of facilities and instrumentation at the UC Irvine Materials Research Institute (IMRI), which is supported in part by the National Science Foundation through the UC Irvine Materials Research Science and Engineering Center (DMR-2011967). W.L., H.L., J.L. and J.-C.Z. are unfunded.

### **Author contributions**

H.L.X. conceived the concept. J.L., J.Z. and H.L.X. co-supervised the project and revised the paper. L.H. designed the experiments and wrote the paper. H.C. performed the XANES and EXAFS fittings and analyses. W.L. and H.L. synthesized the samples. P.O. performed the DFT calculations of formation energy. L.H., R.L., H.W., C.P., C.S., C.W. and W.P. took and analyzed the soft XAS and XAFS spectra. L.H., A.R.H., and X.T. performed the in-situ XPS experiments. All authors discussed the results and implications at all stages.

### **Competing interests**

The authors declare no competing interests.

#### References

- 1. Wu, G., More, K. L., Johnston, C. M., Zelenay, P., High-performance electrocatalysts for oxygen reduction derived from polyaniline, iron, and cobalt. *Science* **332**, 443–447 (2011).
- 2. Qiao, B., Wang, A., Yang, X., Allard, L. F., Jiang, Z., Cui, Y., Liu, J., Li, J., Zhang, T., Single-atom catalysis of CO oxidation using Pt<sub>1</sub>/FeO<sub>x</sub>. *Nat. Chem.* **3**, 634–641 (2011).

- 3. Cui, X., Li, W., Ryabchuk, P., Junge, K., Beller, M., Bridging homogeneous and heterogeneous catalysis by heterogeneous single-metal-site catalysts. *Nat. Catal.* **1**, 385–397 (2018).
- Ji, S., Chen, Y., Zhang, Z., Wang, D., Li, Y., Chemical synthesis of single atomic site catalysts. *Chem. Rev.* 120, 11900–11955 (2020).
- Xiong, Y., Dong, J., Huang, Z.-Q., Xin, P., Chen, W., Wang, Y., Li, Z., Jin, Z., Xing, W., Zhuang, Z., Ye, J., Wei, X., Cao, R., Gu, L., Sun, S., Zhuang, L., Chen, X., Yang, H., Chen, C., Peng, Q., Chang, C.-R., Wang, D., Li, Y., Single-atom Rh/N-doped carbon electrocatalyst for formic acid oxidation. *Nat. Nanotechnol.* 15, 390–397 (2020).
- Wang, Y., Su, H., He, Y., Li, L., Zhu, S., Shen, H., Xie, P., Fu, X., Zhou, G., Feng, C., Zhao, D., Xiao, F., Zhu, X., Zeng, Y., Shao, M., Chen, S., Wu, G., Zeng, J., Wang, C., Advanced electrocatalysts with single-metal-atom active sites. *Chem. Rev.* 120, 12217–12314 (2020).
- 7. Jiang, K., Luo, M., Peng, M., Yu, Y., Lu, Y.-R., Chan, T.-S., Liu, P., de Groot, F. M. F., Tan, Y., Dynamic active-site generation of atomic iridium stabilized on nanoporous metal phosphides for water oxidation. *Nat. Commun.* **11**, 2701 (2020).
- 8. Han, L., Liu, X., Chen, J., Lin, R., Liu, H., Lü, F., Bak, S., Liang, Z., Zhao, S., Stavitski, E., Luo, J., Adzic, R. R., Xin, H. L., Atomically dispersed molybdenum catalysts for efficient ambient nitrogen fixation. *Angew. Chem. Int. Ed.* **58**, 2321–2325 (2019).
- Han, L., Song, S., Liu, M., Yao, S., Liang, Z., Cheng, H., Ren, Z., Liu, W., Lin, R., Qi, G., Liu, X., Wu, Q., Luo, J., Xin, H. L., Stable and efficient single-atom Zn catalyst for CO<sub>2</sub> reduction to CH<sub>4</sub>. J. Am. Chem. Soc. 142, 12563–12567 (2020).
- Han, L., Hou, M., Ou, P., Cheng, H., Ren, Z., Liang, Z., Boscoboinik, J. A., Hunt, A., Waluyo, I., Zhang, S., Zhuo, L., Song, J., Liu, X., Luo, J., Xin, H. L., Local modulation of single-atomic Mn sites for enhanced ambient ammonia electrosynthesis. *ACS Catal.* 11, 509–516 (2020).

- Zhao, L., Zhang, Y., Huang, L.-B., Liu, X.-Z., Zhang, Q.-H., He, C., Wu, Z.-Y., Zhang, L.-J., Wu, J., Yang, W., Gu, L., Hu, J.-S., Wan, L.-J., Cascade anchoring strategy for general mass production of high-loading single-atomic metal-nitrogen catalysts. *Nat. Commun.* 10, 1278 (2019).
- 12. Gu, J., Hsu, C.-S., Bai, L., Chen, H. M., Hu, X., Atomically dispersed Fe<sup>3+</sup> sites catalyze efficient CO<sub>2</sub> electroreduction to CO<sub>2</sub>. *Science* **364**, 1091–1094 (2019).
- 13. Fei, H., Dong, J., Feng, Y., Allen, C. S., Wan, C., Volosskiy, B., Li, M., Zhao, Z., Wang, Y., Sun, H., An, P., Chen, W., Guo, Z., Lee, C., Chen, D., Shakir, I., Liu, M., Hu, T., Li, Y., Kirkland, A. I., Duan, X., Huang, Y., General synthesis and definitive structural identification of MN<sub>4</sub>C<sub>4</sub> single-atom catalysts with tunable electrocatalytic activities. *Nat. Catal.* 1, 63–72 (2018).
- 14. Gao, C., Low, J., Long, R., Kong, T., Zhu, J., Xiong, Y., Heterogeneous single-atom photocatalysts: fundamentals and applications. *Chem. Rev.* **120**, 12175–12216 (2020).
- 15. Ding, S. P., Hulsey, M. J., Perez-Ramirez, J., Yang, N., Transforming energy with single-atom catalysts. *Joule* 3, 2897–2929 (2019).
- 16. Fei, H., Dong, J., Chen, D., Hu, T., Duan, X., Shakir, I., Huang, Y., Duan, X., Single atom electrocatalysts supported on graphene or graphene-like carbons. *Chem. Soc. Rev.* 48, 5207–5241 (2019).
- 17. Yang, H., Shang, L., Zhang, Q., Shi, R., Waterhouse, G. I. N., Gu, L., Zhang, T., A universal ligand mediated method for large scale synthesis of transition metal single atom catalysts. *Nat. Commun.* 10, 4585 (2019).
- 18. Wang, L., Chen, M.-X., Yan, Q.-Q., Xu, S.-L., Chu, S.-Q., Chen, P., Lin, Y., Liang, H.-W., A sulfurtethering synthesis strategy toward high-loading atomically dispersed noble metal catalysts. *Sci. Adv.* 5, eaax6322 (2019).
- Jones, J., Xiong, H., DeLaRiva, A. T., Peterson, E. J., Pham, H., Challa, S. R., Qi, G., Oh, S., Wiebenga, M. H., Pereira Hernández, X. I., Wang, Y., Datye, A. K., Thermally stable single-atom platinum-on-ceria catalysts via atom trapping. *Science* 353, 150–154 (2016).

- 20. Guo, J., Huo, J., Liu, Y., Wu, W., Wang, Y., Wu, M., Liu, H., Wang, G., Nitrogen-doped porous carbon supported nonprecious metal single-atom electrocatalysts: from synthesis to application. *Small Methods* 3, 1900159 (2019).
- 21. Vukmirovic, M. B., Teeluck, K. M., Liu, P., Adzic, R. R., Single Platinum atoms electrocatalysts: oxygen reduction and hydrogen oxidation reactions. *Croat. Chem. Acta* **90**, 225–230 (2017).
- 22. Asakura, D., Hosono, E., Nanba, Y., Zhou, H., Okabayashi, J., Ban, C., Glans, P.-A., Guo, J., Mizokawa, T., Chen, G., Achkar, A. J., Hawthron, D. G., Regier, T. Z., Wadati, H., Material/element-dependent fluorescence-yield modes on soft X-ray absorption spectroscopy of cathode materials for Liion batteries. AIP Adv. 6, 035105 (2016).
- 23. Shannon, R. D., Revised effective ionic radii and systematic studies of interatomic distances in halides and chalcogenides. *Acta Crystallogr.* **32**, 751–767 (1976).
- 24. Walsh, A., Sokol, A. A., Buckeridge, J., Scanlon, D. O., Catlow, C. R. A., Oxidation states and ionicity.

  Nat. Mater. 17, 958–964 (2018).
- 25. Wang, J., Huang, Z., Liu, W., Chang, C., Tang, H., Li, Z., Chen, W., Jia, C., Yao, T., Wei, S., Wu, Y., Li, Y., Design of N-coordinated dual-metal sites: A stable and active Pt-free catalyst for acidic oxygen reduction reaction. *J. Am. Chem. Soc.* 139, 17281–17284 (2017).
- Ren, W., Tan, X., Yang, W., Jia, C., Xu, S., Wang, K., Smith, S. C., Zhao, C., Isolated diatomic Ni-Fe metal-nitrogen sites for synergistic electroreduction of CO<sub>2</sub>. Angew. Chem. Int. Ed. 58, 6972–6976 (2019).
- 27. Gu, J., Hsu, C.-S., Bai, L., Chen, H. M., Hu, X., Atomically dispersed Fe<sup>3+</sup> sites catalyze efficient CO<sub>2</sub> electroreduction to CO. *Science* **364**, 1091–1094 (2019).
- 28. Luo, X., Jean-Charles, R., Yu, S., Effect of temperature on graphite oxidation behavior. *Nucl. Eng. Des.* **227**, 273–280 (2004).
- Zhang, B., Zheng, X., Voznyy, O., Comin, R., Bajdich, M., García-Melchor, M., Han, L., Xu, J., Liu,
   M., Zheng, L., Arquer, F. P. G. d., Dinh, C. T., Fan, F., Yuan, M., Yassitepe, E., Chen, N., Regier, T.,

- Liu, P., Li, Y., Luna, P. D., Janmohamed, A., Xin, H. L., Yang, H., Vojvodic, A., Sargent, E. H., Homogeneously dispersed multimetal oxygen-evolving catalysts. *Science* **352**, 333–337 (2016).
- 30. Qiu, H.-J., Fang, G., Gao, J., Wen, Y., Lv, J., Li, H., Xie, G., Liu, X., Sun, S., Noble metal-free nanoporous high-entropy alloys as highly efficient electrocatalysts for oxygen evolution reaction. *ACS Mat. Lett.* **1**, 526–533 (2019).
- 31. Ding, Z., Bian, J., Shuang, S., Liu, X., Hu, Y, Sun, C., Yang, Y., High entropy intermetallic-oxide core-shell nanostructure as superb oxygen evolution reaction catalyst. *Adv. Sustain. Syst.* **4**, 1900105 (2020).
- 32. Fang, G., Gao, J., Lv, J., Jia, H., Li, H., Liu, W., Xie, G., Chen, Z., Huang, Y., Yuan, Q., Liu, X., Lin, X., Sun, S., Qiu, H.-J., Multi-component nanoporous alloy/(oxy)hydroxide for bifunctional oxygen electrocatalysis and rechargeable Zn-air batteries. *Appl. Catal. B: Environ.* **268**, 118431 (2020).
- Sun, H., Tung, C.-W., Qiu, Y., Zhang, W., Wang, Q., Li, Z., Tang, J., Chen, H.-C., Wang, C., Chen, H.
   M., Atomic metal–support interaction enables reconstruction-free dual-site electrocatalyst. *J. Am. Chem. Soc.* 144, 1174–1186 (2022).

## Methods

**Synthesis.** The monometallic catalysts were synthesized by a dissolution-and-carbonization method. The schematic illustration of the synthetic process is shown in Supplementary Fig. 1. Typically, 144 mg of glucose (C<sub>6</sub>H<sub>12</sub>O<sub>6</sub>) was dissolved in 40 mL of ethanol. Meanwhile, the metal salt precursor (see details in Supplementary Table 1) and 690 mg of hydroxylamine hydrochloride ((NH<sub>3</sub>OH)Cl) were ultrasonically dissolved in 40 mL of deionized water. Subsequently, the ethanol and water solutions were mixed. The mixture was dried in a drying oven at 70 °C for 12 h. Afterwards, it was placed in a crucible, heated from room temperature to 600 °C with a ramp rate of 5 °C min<sup>-1</sup> under Ar atmosphere and kept for 4 h for carbonization. The obtained product was milled into fine powder for further characterization. Exceptionally, since AgNO<sub>3</sub> precursor

can react with Cl<sup>-</sup> in (NH<sub>3</sub>OH)Cl to form AgCl precipitation (Supplementary Fig. 2), the (NH<sub>3</sub>OH)Cl was replaced by tripolycyanamide with the same mole as (NH<sub>3</sub>OH)Cl for the synthesis of Ag SACs. For the synthesis of multimetallic SACs, the procedures are the same as the monometallic catalysts except that multiple metal salt precursors instead of mono ones were added and the weight of each metal precursor was controlled according to Supplementary Table 2.

Moreover, the SACs by the MOF method were synthesized with reference to the reported research<sup>25,26</sup>. Specifically, 2.4 g of 2-methylimidazole was dissolved in 40 mL of methanol by sonication for 5 min. 1.07 g of Zn(NO<sub>3</sub>)<sub>2</sub>·6H<sub>2</sub>O and the given amount of a metal precursor (see Supplementary Table 9 for details) were dissolved in 40 mL of methanol by sonication for 5 min. The two solutions were mixed by magnetic stirring for 12 h. The as-obtained precipitates were centrifuged, washed with methanol several times and dried in vacuum at 70 °C. The dried powder was placed in a tube furnace and then heated to the desired temperature (900 °C) for 3 h at the heating rate of 5 °C min<sup>-1</sup> under flowing Ar gas. Then, it was naturally cooled to room temperature and ground into fine powder to obtain the representative samples. The as-prepared products were directly used without any post-treatment.

Characterization. XRD patterns were collected using an X-ray diffractometer (Rigaku D/max 2500) at a scan rate of 10° min<sup>-1</sup> in the 2θ range of 10°–90°. SEM images were taken on a Verios 460L operated at 20 kV. Atomic-resolution HAADF-STEM images and EDS mappings were taken using an FEI Titan Cubed Themis G2 300 S/TEM with a probe corrector operated at 200 keV and a JEOL JEM-ARM300F Grand ARM S/TEM with double correctors operated at 300 keV. The atomic-resolution HAADF-STEM images were processed by Richardson-Lucy deconvolution (4 iterations)<sup>34</sup> using the DeconvGUI app<sup>35</sup>. Ex-situ XAFS measurements were carried out at

Beamline 7-BM of National Synchrotron Light Source II, Brookhaven National Laboratory, Beamline TPS 44A of National Synchrotron Radiation Research Center, and Beamline 20-BM-B of Advanced Photon Source, Argonne National Laboratory. Soft XAS spectra were collected using both TEY and PFY modes at room temperature in an ultrahigh-vacuum chamber (base pressure, about 10<sup>-9</sup> torr) at the IOS (23-ID-2) beamline of National Synchrotron Light Source II, Brookhaven National Laboratory. Raman spectra were obtained using a high-resolution confocal micro-Raman spectrometer with the model of HORIBA EVOLUTION. Ex-situ XPS measurements were performed on a Kratos AXIS Ultra DLD system with Al-Kα radiation as the X-ray source. TGA measurements were performed on a 209F3A NETZSCH thermal analyzer with a ramp rate of 10 °C min<sup>-1</sup> under N<sub>2</sub> atmosphere. Metal contents of SACs were analyzed by inductively coupled plasma mass spectrometry (Thermo Fishier iCAP RQ ICP-MS).

In-situ XAFS experiments were performed at Beamline 7-BM of National Synchrotron Light Source II, Brookhaven National Laboratory. The precursor mixture of ammonium molybdate, hydroxylamine hydrochloride and glucose for the synthesis of the Mo SAC was pressed and mounted on a holder of a Nashner-Adler reaction cell. The mixture was heated under Ar protection and its XAFS spectra were recorded at given temperatures.

In-situ XPS experiments were performed using a system that counts with an X-ray electron detector (SPECS Phoibos 100MCD analyzer) and an Al-K $\alpha$  X-ray source with a photon energy of 1486.6 eV. The dried precursor mixture of ammonium molybdate or manganese nitrate, hydroxylamine hydrochloride, and glucose for the synthesis of Mo SAC or Mn SAC was pressed on a Cu substrate, transferred to the XPS chamber and heated in ultra-high vacuum. The XPS spectra were recorded at given temperatures.

In-situ soft XAS data were collected with TEY signal on TLS-BL24A beamline, NSRRC. During the measuring, the samples were mounted on the non-oxygen copper plate and heated at given temperatures under high vacuum conditions.

**EXAFS fitting optimization.** The EXAFS data were processed using the Athena and Artemis modules implemented in the IFEFFIT software packages<sup>36</sup>. The raw data of EXAFS spectra were first pre-processed using the Athena module. For each entire spectrum, the pre-edge background absorption was subtracted, and the post-edge was normalized to unity. The data were then transformed from the energy space into the photoelectron momentum vector k space, and a  $k^3$ weighted method was employed to compensate for oscillatory decay. Finally, the R space radial distance spectra were obtained by the Fourier transform of  $k^3$ -weighted  $\chi(k)$  function using a Hanning window. Afterwards, the Artemis module was utilized to extract the local structure information from the spectra by using the least-squares curve parameter fitting method. We have performed a tremendous structure searching for metal SAs and executed EXAFS fitting optimization on each of the potential structural models we found. The atomic distances between center metal atoms and their scattering atoms were initially set to our DFT results and then optimized during the fitting process. Finally, the fitting results with the best EXAFS fitting quality (represented by *R*-factor, the smaller the better) along with the atomic structure models were shown in Fig. 1d and Supplementary Table 4.

**XANES calculation methods.** In this work, we have performed the theoretical XANES calculations to explore the local structure of each single-atom metallic element within the FDMNES package in the framework of a real-space full multiple-scattering (FMS) scheme with the muffin-tin approximation<sup>37,38</sup>. The energy-dependent exchange-correlation potential was

calculated in the real Hedin–Lundqvist scheme, and then the XANES spectra were convoluted using a Lorentzian function with an energy-dependent width to account for the broadening from both the core-hole and final-state widths. A cluster of 7.0 Å radius containing ~70 atoms was used in the calculation with satisfactory convergence being achieved. The structural models for XANES fitting were built based on the EXAFS fitting results and were further optimized by DFT. Quantitative XANES fittings were carried out on each single-atom metallic element to approach the real local structure by optimizing the agreement between calculation and experiment. The fitting qualities were evaluated using the *R*-factor.

**DFT calculations of formation energy.** Spin-polarized DFT calculations using the projector-augmented wave method (PAW) were performed with Vienna ab-initio simulation package  $(VASP)^{39,40}$  with the electron exchange and correlation described by generalized-gradient approximation (GGA) as parametrized by Perdew-Burke-Ernzerhof (PBE)<sup>41</sup>. Plane-wave cut-off energy of 520 eV and a 4 × 4 × 1 Γ-centered k-points grid generated by the Monkhosrt-Pack scheme were used for all calculations. The cell shape and atomic positions in the supercells were fully relaxed until the Hellmann-Feynman forces acting on each atom were less than 0.01 eV Å<sup>-1</sup>. The conjugate gradient algorithm<sup>42</sup> was used for the electronic optimization, and the convergence was considered to be reached when the total energy difference was less than  $10^{-5}$  eV between iterations. For the examined SACs, each of the  $MO_4$  and  $MN_4$  centers was constructed by creating a double vacancy in a 5 × 5 graphene sheet. A vacuum thickness of more than 15 Å was added in the vertical direction to avoid interactions between periodic images. The atomic coordinates of the optimized models are provided in Supplementary Data.

The formation energy  $(E_f)$  of a  $MO_4$  or  $MN_4$  center for SAC is defined as

$$E_{\rm f} = E_{\rm tot} - \sum_{i} \mu_{i} x_{i} \tag{1}$$

where  $E_{\text{tot}}$  is the total energy from DFT calculations, and  $\mu_i$  and  $x_i$  are the chemical potential and quantity of element i in the corresponding SAC, respectively. The  $\mu$  value for a metallic element is referenced to one metal atom in the corresponding bulk crystal, and the  $\mu$  for C, N, and O are taken from one atom in graphene, N<sub>2</sub>, and O<sub>2</sub>, respectively. The correction energies of 0.359 and 0.113 eV/atom were used to correct the energies of O and N atoms, which were obtained by partially fitting the DFT calculated formation energies to the Open Quantum Materials Database<sup>43</sup>. The DFT calculated  $E_f$  of the  $MO_4$  and  $MN_4$  centers are shown in Supplementary Fig. 62.

## Working electrode preparation

The preparation of the working electrode was carried out as follows: a 6 mg catalyst was firstly dispersed in 500  $\mu$ L ethanol. Then, 500  $\mu$ L Nafion solution (0.5%) was added to the suspension, followed by sonication for 1 h to form the homogeneous ink. 200  $\mu$ L of the ink was dropped onto a 1  $\times$  1 cm<sup>-2</sup> carbon paper in four drops and dried at room temperature for electrochemical measurements.

#### **OER** measurement

OER measurements were performed in a three-electrode system (CHI 760E, CH Instrument, USA). A graphitic rod and a mercuric oxide electrode (Hg/HgO) were used as the counter and the reference electrodes, respectively. Electrochemical measurements of the catalysts were measured in 0.1 M KOH solution after purging the electrolyte with N<sub>2</sub> gas for 30 min. Polarization curves were obtained using LSV with a scan rate of 10 mV s<sup>-1</sup>. The long-term stability test was carried out using chronopotentiometric measurements. All potentials measured were calibrated to RHE

using the following Equation: Potential (V vs reversible hydrogen electrode) = Applied potential (V vs Hg/HgO) +  $0.098 \text{ V} + 0.059 \times \text{pH}$ .

## Data availability

The data that support the findings of this study are available within the paper and its Supplementary Information. Source data are provided with this paper. Any other data are available from the corresponding author on request.

### References

- 34. Mkhoyan, K. A., Batson, P. E., Cha, J., Schaff, W. J. & Silcox, J. Direct determination of local lattice polarity in crystals. *Science* **312**, 1354–1354, (2006).
- 35. https://sites.google.com/view/deepem/software-development
- 36. Ravel, B., Newville, M., ATHENA, ARTEMIS, HEPHAESTUS: data analysis for X-ray absorption spectroscopy using IFEFFIT. *J. Synchrotron Radiat.* **12**, 537–541 (2005).
- 37. Joly, Y., X-ray absorption near-edge structure calculations beyond the muffin-tin approximation. *Phys. Rev. B* **63**, 125120 (2001).
- 38. Bunău, O., Joly, Y., Self-consistent aspects of x-ray absorption calculations. *J. Phys. Condens. Matter* **21**, 345501 (2009).
- 39. Kresse, G., Hafner, J., Ab initio molecular-dynamics simulation of the liquid-metal-amorphous-semiconductor transition in germanium. *Phys. Rev. B* **49**, 14251–14269 (1994).
- 40. Kresse, G., Furthmüller, J., Efficiency of ab-initio total energy calculations for metals and semiconductors using a plane-wave basis set. *Comp. Mater. Sci.* **6**, 15–50 (1996).
- 41. Perdew, J. P., Burke, K., Ernzerhof, M., Generalized gradient approximation made simple. *Phys. Rev. Lett.* **77**, 3865–3868 (1996).

- 42. Payne, M. C., Teter, M. P., Allan, D. C., Arias, T. A., Joannopoulos, J. D., Iterative minimization techniques for ab initio total-energy calculations: molecular dynamics and conjugate gradients. *Rev. Mod. Phys.* **64**, 1045–1097 (1992).
- 43. Kirklin, S., Saal, J. E., Meredig, B., Thompson, A., Doak, J. W., Aykol, M., Rühl, S., Wolverton, C., The Open Quantum Materials Database (OQMD): assessing the accuracy of DFT formation energies. *NPJ Comput. Mater.* **1**, 15010 (2015).